Simple and Accurate Empirical Absolute Volume Calibration of a Multi-Sensor Fringe Projection System

Munther Gdeisat[a,], Mohammad Qudeisat[b], Mohammed AlSa'd[c], David Burton[d] and Francis Lilley[d], Marwan M. M. Ammous[a]*

[a]Colleges of Applied Sciences, Sohar, PO BOX 135, Post Code 311, Oman, E: gdeisat@hotmail.com

[b]Purdue University, Department of Computer Science, 305 N. University Street, West Lafayette, IN 47907-2107, USA.

[c]University of Cambridge, Rutherford Building, Cavendish Laboratory, University of Cambridge, Cambridge, CB3 0HE, U.K.

[d]Liverpool John Moores University, General Engineering Research Institute, Liverpool L3 3AF, United Kingdom

Abstract

This paper suggests a novel absolute empirical calibration method for a multi-sensor fringe projection system. The optical setup of the projector-camera sensor can be arbitrary. The term absolute calibration here means that the centre of the three dimensional coordinates in the resultant calibrated volume coincides with a preset centre to the three-dimensional real-world coordinate system. The use of a zero-phase fringe marking spot is proposed to increase depth calibration accuracy, where the spot centre is determined with sub-pixel accuracy. Also, a new method is proposed for transversal calibration. Depth and transversal calibration methods have been tested using both single sensor and three-sensor fringe projection systems. The standard deviation of the error produced by this system is 0.25 mm. The calibrated volume produced by this method is 400 mm × 400 mm × 140 mm.

Keywords: depth calibration, transversal calibration, empirical calibration, absolute calibration, multi-sensor fringe projection systems.

1. Introduction

The goal of fringe projection measurement systems is to measure the 3D shape of objects. Phase measuring fringe analysis techniques typically produce phase distribution information with units of phase in radians. A calibration process is required in order to convert this phase information into 3D information in physical units of distance, such as millimetres.

1

Calibration methods can be classified as being either relative or absolute. Relative calibration techniques produce 3D information that determine the distance between any two points on the object's 3D shape map, but it does not tie these points to a reference point within the real world. Conversely, absolute calibration techniques produce 3D information that is tied to a known location in terms of real-world coordinates. Full calibration of fringe projection systems requires calibrating both depth (Z) and transversal (X, Y) axes.

1.1 Depth Calibration Techniques

The goal of the depth calibration process is to find a transformation function that can transform the phase map that is produced by fringe analysis methods into a depth map. There are many calibration algorithms that have been proposed for fringe projection measurement systems. Each algorithm uses a different method to establish the phase-to-depth transformation. The depth calibration methods generally fall into three different categories:

1. Analytical or model based methods: These methods analyse the geometry of the fringe projection system in order to establish an explicit mathematical phase-to-depth transformation. The analytical model that is produced by these methods includes the extrinsic system parameters (such as the camera & projector geometrical layout) and intrinsic system parameters (such as the camera's and projector's focal lengths, pixel sizes, etc.). These parameters must be determined with very high accuracy in order for it to be possible for the overall calibrated system to produce accurate measurements [1].

2. Hybrid methods: These methods aim to improve the accuracy of the estimated system parameters by creating an analytical model of the system with initial estimations of the system parameters, subsequently using empirical data in order to improve the accuracy of the estimated system parameters [1].

3. Empirical or polynomial methods: These methods gather empirical data from the measurement system and they establish a direct phase-to-depth mapping function depending on the data that is gathered. The extrinsic and intrinsic system parameters are automatically contained within the gathered data and need not be explicitly included within the system model [1].

These categories of depth calibration algorithms have different performance characteristics. For example, analytical methods tend to be very complex and they sometimes produce unstable results, such as divide-by-zero expressions. Moreover, the accuracy of these analytical methods is very sensitive to the accuracy of the estimated system parameters [1, 2, 3]; even a tiny error in estimating one system parameter can adversely affect the accuracy of the final system measurements. These methods usually contain presumptions, or impose restrictions upon the optical geometry of the system in order to simplify the mathematical model which is produced. Such issues limit their flexibility in terms of the geometric model of the system. For example, in Zhu's model the camera and the projector must be placed at the same height [4]. Zhu seems to oversimplify the calibration model into a linear least-squares relationship and his results are produced for a relatively small depth calibration range (of around 30 mm). As suggested by Jia et al., the linear system models are normally valid for small calibration ranges [5]. Le´andry et al. have developed a calibration algorithm to measure large objects such as human body [6]. The overall calibration process for these methods, however, takes a considerably shorter time than is the case for the empirical methods.

Another problem that is associated with the analytical models is the great difficulty that is associated with correctly identifying and modelling all of the system's intrinsic and extrinsic parameters. For example, the fact that the camera lens distortion factor actually varies spatially from pixel to pixel at different spatial CCD array locations, so if a global distortion factor for the camera lens is used, then this can limit the accuracy of the measurements that are produced. This problem is best reflected by Tian's [7] 3D measurement technique, where he concludes at the end of his paper that the accuracy of his method is mainly limited because of the inferior accuracy of his camera distortion model. In his paper he used a radial distortion model, but it turned out to be relatively inaccurate. Moreover, the fact that different cameras might have very different designs, and hence potentially very different mathematical models, leads to scalability and portability problems. Because of these issues, even if a mathematical model very accurately describes the intrinsic parameters of the hardware components, it may well fail completely if the camera is replaced with a different model. This means that mathematical calibration methods need to be refined every time the system hardware is changed. Such methods are therefore less likely to be portable when applied to systems employing different hardware components. Additionally, the

3

existence of a projector complicates the analytical model and some authors have attempted to exclude it to simplify the analytical calibration process [8].

Hybrid methods have appeared as a result of attempts to achieve the best of both the analytical and empirical calibration approaches. Hybrid methods are slightly less complex to implement than analytical calibration approaches and remain potentially unstable. However, they provide greater accuracy in estimating the system parameters than is the case for purely analytical methods, and they give consequently more accurate measurements [9].

Empirical methods are much simpler to implement than either analytical or hybrid methods, and stable results are almost always guaranteed. They are also comparatively less sensitive to the accuracy of the empirical calibration data that is acquired (than is the case for the relatively higher sensitivities that are exhibited by the analytical methods) to inaccuracies in the estimated system parameters. However, the system calibration process is usually relatively time-consuming.

Empirical calibration methods are generally performed by capturing a series of fringe patterns for a flat surface that is placed at different known depths (d_0, d_1,…,d_n), and then a direct phase-to-depth relationship is established, usually using polynomial fitting [10], or interpolation [11]. For some of the proposed methods, each camera pixel is calibrated individually and locally using its own data [10], whereas in other methods the phase-to-depth transformation is established globally for all camera pixels [11]. Generally, local calibration methods produce better results than their global counterparts.

Empirical methods are time consuming. Generally, empirical methods need to acquire fringe patterns that are projected onto a large number of parallel planes (around 50, in Liu's [10] method) at known depth values [12]. Anchini *et al.* [13] and Zhang *et al.* [14] have suggested the use of virtual phase approaches to acquire fringe data for only a few parallel planes (typically two, or three) and then to generate fringe data for virtual planes, where the data for the "virtual planes" has not been actually acquired by the system, but is instead estimated by various proposed techniques. The virtual phase method has succeeded in greatly reducing the required

time for the calibration process, but it requires estimating the intrinsic and extrinsic system parameters, and this increases the complexity of the calibration procedure.

One good example of the adverse effects of overly reducing the number of calibration planes manifests clearly in D'Argenio's paper [15], where he reduces the number of the required calibration planes to only two. He also uses a pinhole model for the camera, which proved to be inaccurate in most cases. In his work, D'Argenio concludes that his method results in a maximum error of 2.5% of the total depth calibration range. This error can be considered to be very large in this context. Zappa et al. have proposed a calibration method without the need to place the calibration volume at different height levels with high accuracy. This eliminates the need of high accurate positioning systems [16].

Liu *et al.* [10] proposed a mathematical equation describing the phase-to-depth relationship, as is expressed in Eq. (1).

$$z = \frac{m_1^{'}\varphi + m_0^{'}}{n_1^{'}\varphi + 1} + \sum_{0 \le i \le 6}\left[\frac{g_i - h_i\varphi}{n_1^{'}\varphi + 1}\left(\frac{m_1^{'}\varphi + m_0^{'}}{n_1^{'}\varphi + 1} \right)^i \right] \tag{1}$$

Where:

φ: The unwrapped phase value. And $m_1^{'}, m_0^{'}, n_1^{'}, g_i, h_i$ are constants.

The first term represents the ideal phase-to-depth relationship, whereas the latter part originates from distortions within the captured image. They have suggested a fifth-order polynomial fitting method to approximate the phase-to-depth relationship for every camera pixel. This calibration method has the following advantages. Each and every pixel is calibrated using only its own data. Also, it is suitable for use with virtually any optical system configuration. Additionally, it enables absolute depth measurement to be performed and the calibration procedure can be fully automated.

1.2 Transversal Calibration Techniques

Transversal calibration methods can generally be divided into two main categories:

1. Photogrammetry methods**: which are generally based upon the determination of the intrinsic and extrinsic properties of the camera sensor in order to find the geometric properties of the objects from their photographic images [17,18].
2. Empirical methods that aim to find a direct mapping between the camera's coordinate system and the world coordinate system. Methods that fall into this category generally use a calibration grid upon which points of known XY world coordinates are marked. Then, by determining the exact locations of these grid points a mapping relationship is found between the camera's coordinate system and the world coordinate system [10, 12].

Tsai [17] has proposed one of the most well-known and effective photogrammetric methods for achieving absolute transversal camera calibration. His method is based on recording a series of images for a chessboard grid at different known depths. This method is known to be one of the most accurate photogrammetric methods; however, it does have two shortcomings: First, it has a low spatial sampling density; only forty-nine points are used to calibrate the transversal directions of the whole image. This means that most pixels are calibrated using interpolated data from neighbouring pixels, which negatively affects the accuracy of the results and causes errors to propagate throughout the image. Secondly, the automatic detection of the corners is not very reliable. Sometimes human assistance is needed to help the computer determine the locations of the corners which can sometimes make the calibration process very time-consuming.

Stinik [19] has also described a transversal calibration model where he uses equidistant circles that are printed on a planar surface in order to estimate the transversal coordinates of each point on the object image. His method has the disadvantage of having a low spatial sampling density.

Liu *et al.* analysed the relationship between the absolute physical transversal coordinates (X and Y) and the depth Z [10]. They have found that for any particular pixel in the camera's CCD array the relationship between the transversal coordinates X and Y and the depth (Z) is linear as expressed in Eqs. (2).

$x = a_1 d + a_0$ (2a)

$y = b_1 d + b_0$ (2b)

Where:

x and y are the absolute physical transversal coordinates.

z is the absolute physical depth.

a_0, a_1, b_0 and b_1 are constants that are to be determined for every camera pixel.

Liu *et al.* suggested using a printed fringe pattern on a plane surface for transversal calibration [10]. The printed fringe patterns shown in Figs. 1(a) and 1(b) are used one after the other in a serial manner in order to calibrate the X and Y axes respectively.

The Fourier transform method can be used to extract the phase of each of the fringe patterns and then relate the extracted relative phase to relative X and Y coordinates. In this paper we suggest combining both fringe patterns by arithmetic addition in order to produce a single composite XY calibration pattern, so as to reduce the calibration time. The combined fringe pattern is shown in Fig. 1(c). The combined fringe pattern is printed on 1cm thick float glass and captured using a camera and the captured image is shown in Fig. 1(d). The Fourier transform algorithm in [20] can be used to process this captured image in order to extract the two unwrapped phase maps for the X and Y axes respectively.

The modifications to Liu's method by combining fringe patterns will enable the system to produce absolute transversal measurements and will also reduce the required calibration time by 50%. It will also remove problems inherent with Liu's original method that are associated with inaccurately re-locating the second sinusoidal fringe pattern in exactly the same position as the first pattern and at an exactly orthogonal orientation

The main disadvantage of this method is that it is not easy to use it for absolute calibration. The authors suggest a further modification of Liu's method as explained in Section 5.

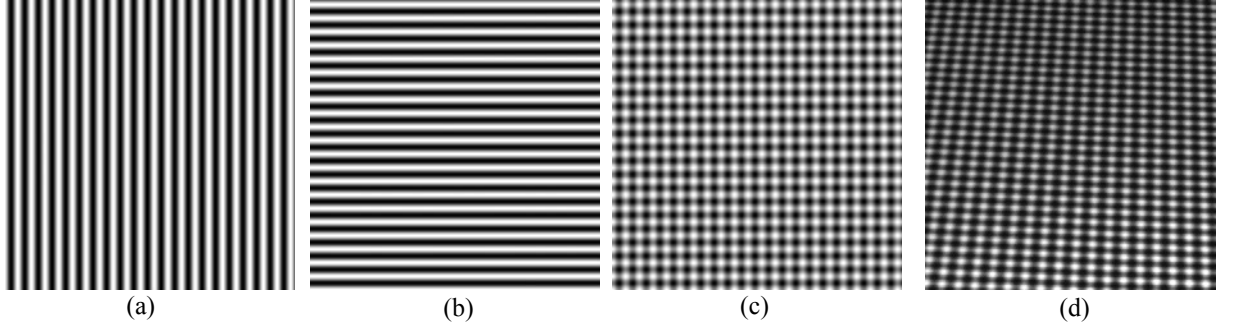<div align="center">(a)   (b)   (c)   (d)</div>

Fig. 1 Liu's *et al.* transversal calibration method (a) and (b). The author's proposed combined method (c) and (d).

The authors have also extended Liu's method in order to make it suitable for absolute transversal calibration. We have added a double period fringe at the centre of the printed glass plate. These double-period fringes are used to mark the absolute physical X and Y axes, which will enable the proposed system to produce absolute transversal measurements as explained in Section 5.

Section 2 in this paper explains the three-sensor fringe projection system that is used to implement and evaluate the proposed depth and transversal calibration methods. This depth calibration is discussed in Section 3; whereas evaluation of the proposed depth calibration is discussed in Section 4. Section 5 explains the proposed transversal calibration technique. Sections 6 and 7 evaluate calibration methods using both single and three-sensor fringe projection systems respectively.

2. Three-Sensor Fringe Projection System

The fringe projection system used here to implement and test the proposed absolute calibration algorithm consists of three sensor units, with each sensor unit consisting of a pair of one camera and one projector. A Canon XEED SX60 projector has been adopted for this fringe projection system and it has the resolution of 1600×1200 pixels. Prosilica GE1380 has been used here and it has the speed of 35 frames per second at 512×512 pixels resolution.

Each sensor unit works on a unique light bandwidth which is achieved via RGB optical colour filters that are attached to both the camera and projector lenses, with a pair of the same colour filters being attached to each one of the three sensor pairs. Optical colour filters XB24, XB21,

XB08 [21] are attached to the camera and projector of the red, green and blue sensor pairs respectively. Each sensor is connected by Ethernet cables to its own data processing unit and all data processing units are connected to a main server that coordinates and controls the operation of the three sensors. Figs. 2(a) and 2(b) show the components and layout of the system.

As the system consists of three sensor heads, it is necessary to minimise any potential chance for crosstalk amongst the sensors, and so each camera and projector set are fitted with colour separation filters. The colour filters on each sensor head enable simultaneous projection of the three different RGB coloured fringe patterns onto the object and ensures that each camera grabs only the intensity modulation of the correctly associated projector, without affecting the functionality of the other sensor heads. An additive colour separation model is adopted for the system using the primary colours: red, green and blue. The system performance, in terms of using multi-sensor profilometry, crucially depends on the degree of eliminating any overlapping wavelengths between the colours as well as the following characteristics of the chromatic filter:

- Centre Wavelength (CWL): which is the wavelength at the centre of the pass-band filter, that should be matched by the wavelength of each projected colour.
- Full Width at Half Maximum (FWHM): is the bandwidth at 50% of the maximum transmission. At this bandwidth there should not be any overlap between colour wavelengths.
- Peak Transmission (PT): it is the wavelength of maximum transmission, higher PT gives higher sensitivity and quantum efficiency.

The adopted filters have been carefully selected to eliminate any effect of colour crosstalk on the resultant measurement. Fig. 2(c) shows the resultant spectrum when applying the colour pass-band filters and Fig. 2(d) shows the characteristics of the adopted filter.

The system is designed to produce absolute three-dimensional physical measurements that cover a 400 mm × 400 mm transversal field of view and a vertical range of at least 140 mm, with a maximum mean depth and transversal measurement error of 0.5 mm and a maximum standard deviation of 0.25 mm. All three sensors are required to use a unified real world coordinate system. Each sensor measures an object from a different angle independently from the other

sensors in the system and synchronization logic is implemented so that all sensors take their measurements synchronously. Measurements from different sensors are then sent to the main server to be merged and used for the construction of the final object's full 3D profile.
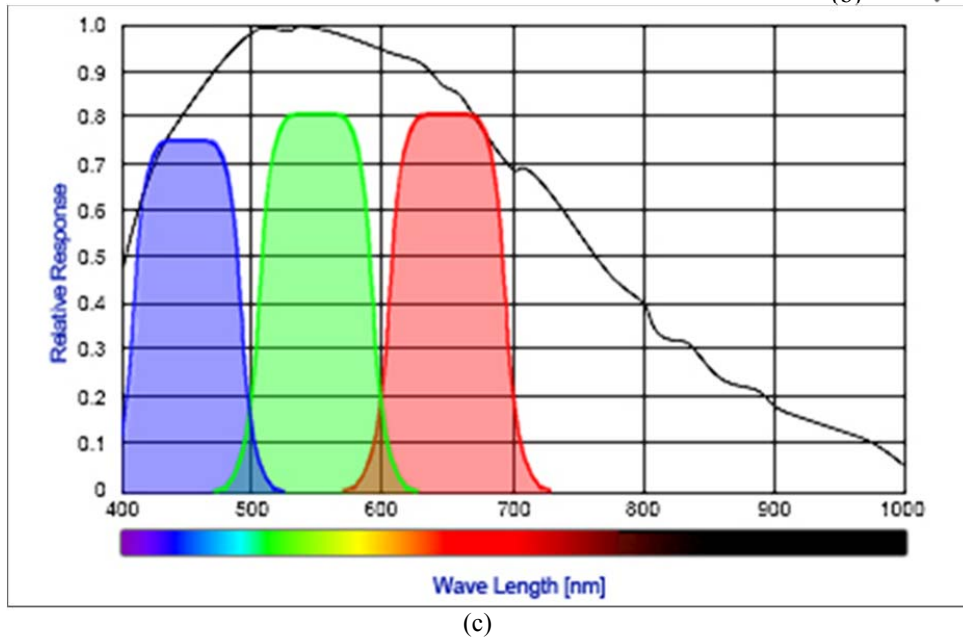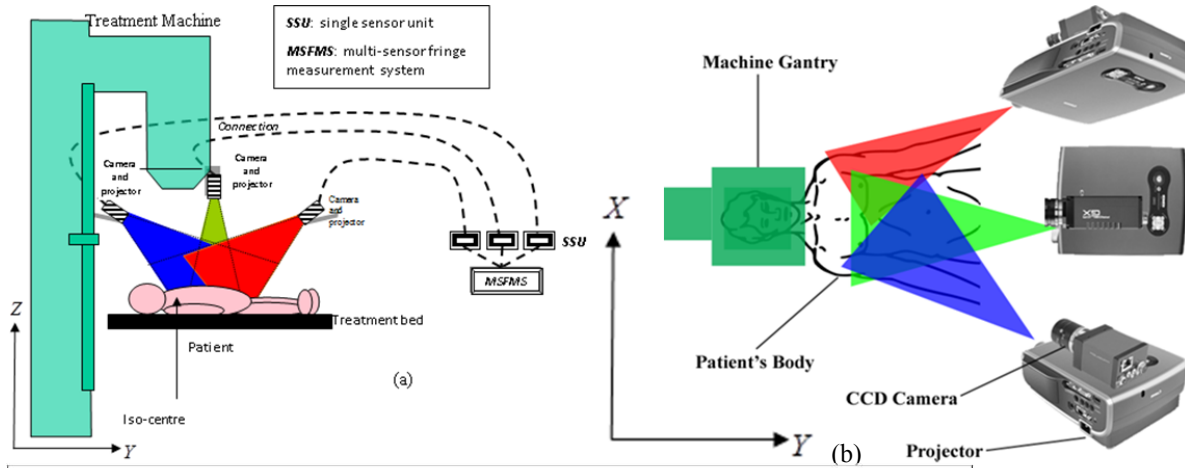
Colour Filter	Bandwidth (FWHM) [nm]	CWL [nm]	PT (Transmission) [%]
Red: Horiba XB24	80	650	80
Green: Horiba XB21	80	550	80
Blue: Horiba XB08	80	450	75

(d)

Fig. 2 (a) and (b)the layout and the components of a three sensor fringe projection system. (c) and (d) the optical characteristics of the chromatic filters.

3. Absolute Depth Calibration

Absolute depth calibration refers to the process of converting the unwrapped phase map of a fringe pattern into depth information tied to the Z real world coordinate system. Absolute also implies that the origin point of the proposed measurement system's coordinate system must be mapped to a known reference point in the real-word.

The depth calibration process starts by determining the centre of the real world coordinates. This is an important issue since the depth calibration proposed here is absolute. Here we have used the intersection of three laser beams that are fixed to three perpendicular walls in order to determine this central datum, as shown in Figs. 3(a) and 3(b). The steps below explain the proposed depth calibration algorithm for a one-sensor fringe projection system on a step-by-step basis. This algorithm may be extended to the multi-sensor fringe projection system as described in Section 7.

3.1 Calculation of the relative phase map

In this step, a white planar glass platten is set at the absolute depth Z=0 mm as shown in Fig. 3(b), and then it is levelled using a precise digital inclinometer (*i.e.,* inclination angle $\cong 0^{\circ}$). Four fringe-pattern images with a phase shift of $\pi/2$ between each two successive images are then generated using a computer and then they are projected onto the white plane successively. These four fringe patterns, shown in Figs. 2(c) to (f), have a size of 512 × 512 pixels and are generated using Eq. (3). The spatial carrier frequency f_o is set here to 1/24. The number of pixels per fringe (period) must be divisible by 4 and it is set here to 24. The constant "1" is added in order to ensure that all the pixels in the computer-generated fringe patterns always have positive intensity values.

$$I_1(x,y) = 1 + \cos(2\pi f_o x) \tag{3a}$$
$$I_2(x,y) = 1 + \cos(2\pi f_o x + \frac{\pi}{2}) \tag{3b}$$
$$I_3(x,y) = 1 + \cos(2\pi f_o x + \pi) \tag{3c}$$
$$I_4(x,y) = 1 + \cos(2\pi f_o x + \frac{3\pi}{2}) \tag{3d}$$

The four fringe patterns are captured using a monochrome camera and the phase is extracted using the four-frame phase stepping algorithm [22].

$$\emptyset(x,y) = tan^{-1}\left(\frac{I_1 - I_3}{I_4 - I_2}\right) \qquad (4)$$

The extracted phase that is produced is wrapped $\emptyset(x,y)$ and this can be unwrapped by using a basic phase unwrapping algorithm [23], or by eliminating the wraps as explained in [24], or more sophisticated phase unwrapping methods [25, 26, 27, 28]. This produces a relative unwrapped phase distribution, which is required to be converted to an absolute unwrapped phase using the zero-phase fringe-marking spots, as explained below.

3.2 Calculation of the absolute phase map using zero-phase fringe-marking spots

3.2.1   *Calculating spot centre with pixel accuracy*

A five-spot image with a size of 512×512 pixels is constructed using the computer and this is shown in Fig. 3(g). The values of all the pixels in this image are set to "0" except for the pixels in the five spots whose values are set to "2". Each spot consists of a 5×5 pixel region. The centres of the five spots are aligned exactly with the valley of a fringe; hence they and are set on the same horizontal line. This is to ensure that all the pixels in the unwrapped phase map that correspond to the spots' centres have the same phase value. Also, this simplifies extracting the spot in the case when it is embedded in a fringe pattern, since all the pixels surrounding the spot should have lower intensity values than the spot. The number of pixels per fringe in the projected fringe pattern is set here to 24, so there is a pixel with exactly zero phase value and it locates exactly at the valley of the fringe. This pixel is set to coincide exactly with the centre of the spot. Hence, the location of the spot centre coincides exactly with a wrap in the wrapped phase map.

These spots can be embedded in a fringe pattern. This can be carried out by the arithmetic addition of the fringe pattern image shown in Fig. 3(c) to the spot image that is shown in Fig. 3(g). After the addition process, the pixels whose values are greater than "2" are set to "2". This clipping process is to ensure that fringes in the image will not fade out. The resultant image is shown in Fig. 3(h).

The five-spot image is projected onto the white plane and then captured by the camera. The captured image is shown in Fig. 3(i). The captured image is thresholded. This will give five blobs that correspond to the five spots. The centre of each of these blobs is then estimated with pixel accuracy as follows [29]. The X coordinate of the estimated spot centre is equal to the average of the X coordinates of the pixels whose values are larger than the threshold in the blob. Similarly, the Y coordinate of the estimated spot centre is equal to the average of the Y coordinates of the pixels whose values are larger than the threshold in the blob.

3.2.2 Calculating spot centre with sub-pixel accuracy

A method to determine the centre of each of the spots with sub-pixel accuracy is explained here as follows. The centre of a spot coincides exactly with a 2π phase jump (a wrap) as shown in Fig. 3(j). The phase wrap coincides with the valley of a fringe. The phase value at the phase jump is known to have a value of π. So we need to find the sub-pixel location that corresponds to this π value. This is carried out by initially estimating the spot location with pixel accuracy as explained above. Then we search for the nearest phase wrap and find the exact location with sub-pixel accuracy at which the phase value is equal to $+\pi$. This is carried out by adding a 2π value to the pixel to the right of the wrap. Then the location of spot with sub-pixel accuracy is determined using linear interpolation as explained using the following numerical example.

Let the centre of the spot is estimated with pixel accuracy as (100, 49). Also, let the nearest wrap be located between the pixels with indices (100, 50) and (100, 51). The pixel to the left of the phase wrap has the index (100, 50) and a value of 0.9π. Also the pixel to the right of the phase wrap has the index (100, 51) and a value of -0.95π. A value of 2π is added to the pixel to the right and its new value will be 1.05π. Now the spot centre sub-pixel may be determined with sub-pixel accuracy as follows. The equation of the line connecting the two pixels is $y = mx + b$. The slope of the line is calculated as $m = (1.05\pi - 0.9\pi)/(51 - 50) = 0.15\pi$. The intersection with the y axis is calculated as $b = 0.9\pi - 0.150\pi(50) = -6.6\pi$. The spot centre with sub-pixel accuracy is $(\pi + 6.6\pi)/0.15\pi = 50.667$. The location of the spot centre is therefore (100, 50.67).

3.2.3   Converting the relative phase into absolute phase using the spots

After that the value of the unwrapped phase at the spot centre, with sub-pixel accuracy, is determined by using linear interpolation.

The process of estimating a spot centre, initially with pixel accuracy, and then with sub-pixel accuracy, is repeated for the other four spots. After that the value of the unwrapped phase map at the spot centre is determined with sub-pixel accuracy using linear interpolation.

Ideally all the five unwrapped phase values that correspond to the five spots' centres with sub-pixel accuracy should be equal because they are all located on the valley of the same fringe. But due to noise these values could exhibit slight deviations, for example by a threshold of 0.1π. The average of the five phase values is therefore calculated and subtracted from the unwrapped phase map. This step converts the relative unwrapped phase extracted by the phase stepping algorithm to an absolute unwrapped phase map.

It could be possible that one phase value may be significantly different than the other four values (different from the other phase values by more than the preset threshold). In this case, this deviated phase value will be excluded from calculating the average phase.

3.2.4   Repetition of the depth calibration algorithm for different depth values

The first and second steps are now repeated for another absolute depth value, for example Z=10 mm. A white planar glass platten is moved to the depth Z=10 mm. Then the same four fringe pattern images are projected and the wrapped and the relative unwrapped phase map is calculated. After that the same computer-generated image that contains the five spots is projected and the location of the spots' centres sub-pixel is determined with sub-pixel accuracy. Then the absolute unwrapped phase is determined for this depth. It is important to emphasize that the same fringe patterns and spots' image used with depth Z=0 mm must be used here for this new depth value.

The process above is repeated for various different absolute depth values. In this experiment, depth values with Z=20, 30, 40, …140 mm are used. Changing the depth values can be carried

out either manually, or automatically. A computer-controlled high-precision elevator table was used here to change the depth automatically. This elevator table, shown in Fig. 3(k), is from LG Motion Ltd and employs a ViX micro-step drive which can be controlled by sending commands through a RS232 serial cable. The elevator table machine can lift a maximum load of 50 kilograms which is more than enough to lift the calibration glass, which weighs around 25 kilograms. The depth accuracy for this elevator is 1μm [30].

A lookup table that relates absolute depth values to the absolute unwrapped phase values for each pixel can subsequently be constructed. This calibration process produces $512 \times 512 = 262,144$ lookup tables, and each lookup table has 15 entries, since calibration has been carried out using 15 depth values. One of these lookup tables is shown as a 2D plot in Fig. 3(l).

The lookup tables for contiguous pixels are very similar and this information can be used to reduce noise. So the calibration volume can be processed using a $3 \times 3 \times 3$ median or smoothing filters. This should alleviate the effect of data produced by dead pixels, impulsive and white noises.

3.2.5 Spots' trajectories

The calibration process for each absolute depth value produces five spots' centres with sub-pixel accuracy. These five values are converted into integers using the rounding operation. For example, the centre for one of the spots is (100, 51) for the absolute depth Z=0. The above process is repeated for all the calibrated depth values. This produces $5 \times 15 = 75$ centres. An image with the size of 512×512 pixels is constructed. The values of all the pixels are set to zero except the spots' centres where the values are set to "1". The resultant binary image is shown in Fig. 3(m). This image shows the trajectories that the spots' centres' follow during the variation in the depth values for the calibrated volume. This binary image is dilated using a 5×5 element and the resultant dilated binary image is shown in Fig. 3(n).

The above procedures can be carried out to calibrate the depth of the three sensors either simultaneously, or on a one-by-one basis. These procedures have been used here to calibrate the

three sensors in the fringe projection system both simultaneously and fully automatically without any manual intervention.

During the measurement process, the spots will be located on the trajectories that are generated during the calibration process. So searching for the spots during measurement will be limited to the regions corresponds to these trajectories. This reduces errors in determining spots' locations during the measurement process. A simple method is to multiply the fringe pattern captured to measure an object by the spots' trajectories dilated binary image shown in Fig. 3(n). Then we search for spots in the resultant image.
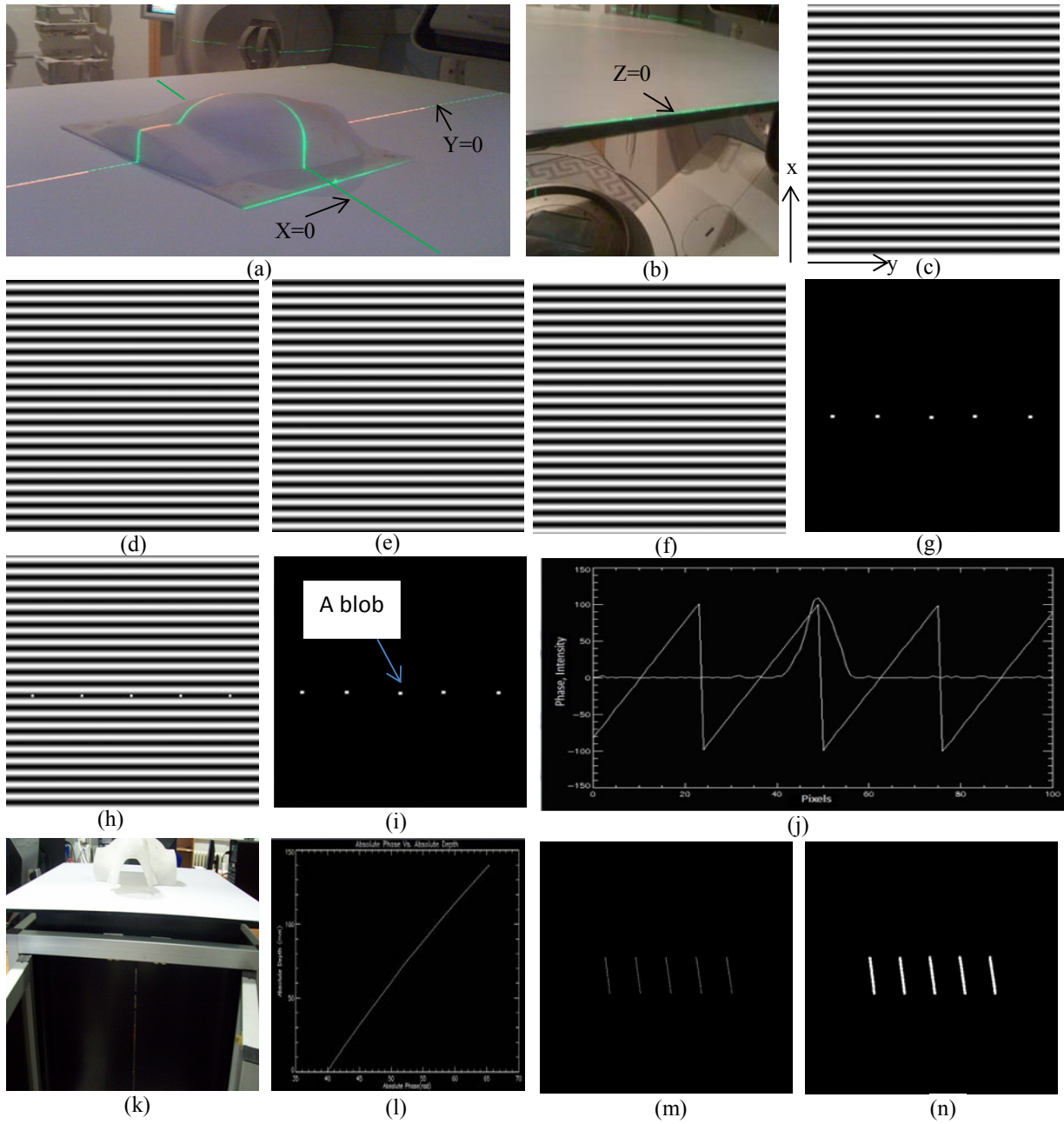
(a)

(b)

(c)

(d)

(e)

(f)

(g)

(h)

(i)

(j)

(k)

(l)

(m)

(n)

Fig. 3 The procedure to calibrate the depth of a fringe projection system.

4. Evaluation of Absolute Depth Measurement Accuracy

A simple method to evaluate the proposed calibration algorithm is to measure a planar surface that is set at a specific depth and has a zero inclination angle. The planar glass platten has here been adjusted to the absolute depth $Z = 7$ mm. A fringe pattern that contains five embedded spots in a fringe, shown in Fig. 3(h), is projected onto the platten. Then the fringe pattern is captured by a camera and the captured image is shown in Fig. 4(a).

Initially, the location of the spots' centres should be determined with pixel accuracy. To perform this task the fringe pattern is smoothed using a 5×5 filter. This filter washes out any bright spots that are smaller than the filter size as they are likely to appear as a result of camera noise. However, the filter will not be able to remove larger bright spots as the filter size is chosen to be smaller than the estimated spot size. Then a second order differentiation Laplacian filter [31] of size 2×2 is applied to the smoothed image. This filter is used for edge detection and the resultant image is shown in Fig 4(b). After that a kernel filter of size 6×6, shown in Fig. 4(c), is applied to the image. Finally the filtered image is multiplied by the dilated spots' trajectories as a binary image, shown in Fig. 3(n). The resultant image is shown in Fig. 4(d), which is then thresholded in order to determine the spot location with pixel accuracy. Then the spots' centres are determined with sub-pixel accuracy as explained in the depth calibration section.

The fringe pattern image shown in Fig. 4(a) is demodulated using the Fourier transform method and the resultant wrapped and unwrapped phase maps are shown in Figs. 4(e) and 4(f). The distortion due to the spot is clear and it should be removed by restoring the original fringe pattern as follows.

To restore the fringe pattern shown in Fig. 4(a), the fringe pattern is filtered using a 3×3 median filter in order to remove salt-and-pepper noise in the image [31]. Then the value of each pixel within the spot is replaced by an interpolation of the horizontally adjacent pixels of the surrounding fringe pattern. The result of this step for the centre spot is shown in Fig. 4(g). The other four spots are removed using the method explained for the middle spot and the resultant image is shown in Fig. 4(h). The restored image is analysed using the 2D Fourier transform, and the resultant wrapped and unwrapped phase maps are shown in Figs. 4(i) and 4(j). The relative

unwrapped phase is converted to absolute phase using the locations of the spots' centres with sub-pixel accuracy and via linear interpolation, as explained above. The absolute unwrapped phase value for a specific pixel is then converted to absolute depth information using linear interpolation by employing the depth calibration lookup table that was constructed during depth calibration for that pixel. This process is repeated for all the pixels in the absolute unwrapped phase map. The resultant absolute depth information map for the planar glass platten is shown in Fig. 4(k) and it has a mean of 7.182 mm and a standard deviation of 0.135 mm.

The use of planar surface allows checking the calibration at a specific height, but it does not report any errors may be produced by the calibration algorithm at other heights. The planar surface does not completely evaluate the calibration method and it is used here only for simplicity.

The reader should notice that same fringe pattern used for depth calibration must be also used for the depth measurement. Although the depth calibration process is carried out using phase stepping, other algorithms can be used to extract the phase such as the Fourier transform method.

A separate image can be used to project the fringe marking spots or they can be embedded inside the fringe pattern. The former method is more accurate but the latter technique requires one image fewer and so is faster.

The number of fringe marking spots to be used in calibration or measurement is optional. For example, one spot could be used during the depth calibration process and five, or more, spots during the measurement process, or vice versa. Increasing the number of spots increases noise tolerance.

During depth measurement, it may occur that one of the spots is located on an edge or discontinuity upon the object and it may split into two spots as shown in Fig. 4(l). In these cases the spot can be excluded from the calculation of the average as explained above.
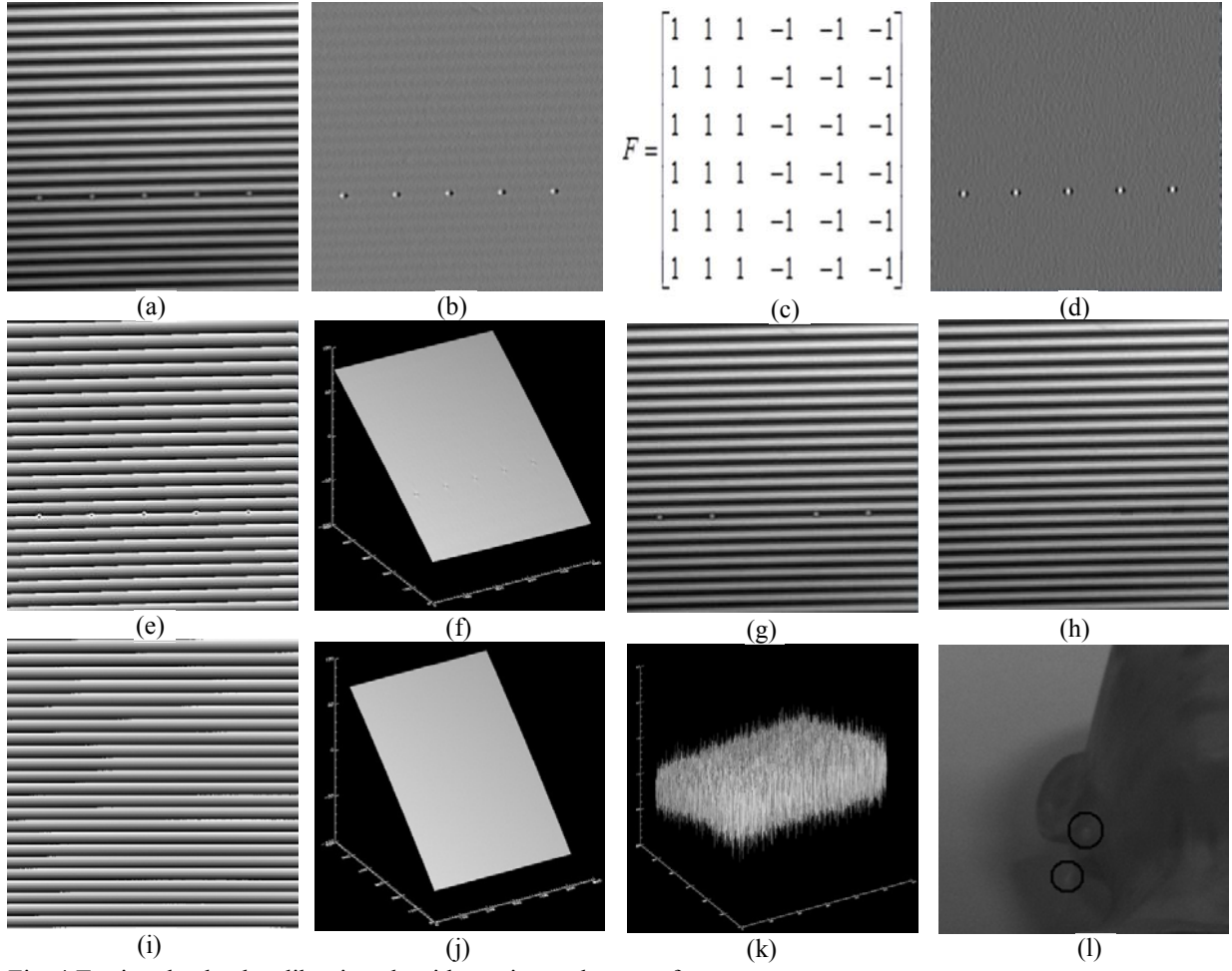
$$F = \begin{bmatrix} 1 & 1 & 1 & -1 & -1 & -1 \\ 1 & 1 & 1 & -1 & -1 & -1 \\ 1 & 1 & 1 & -1 & -1 & -1 \\ 1 & 1 & 1 & -1 & -1 & -1 \\ 1 & 1 & 1 & -1 & -1 & -1 \\ 1 & 1 & 1 & -1 & -1 & -1 \end{bmatrix}$$

(a)　　　　　　(b)　　　　　　(c)　　　　　　(d)

(e)　　　　　　(f)　　　　　　(g)　　　　　　(h)

(i)　　　　　　(j)　　　　　　(k)　　　　　　(l)

Fig. 4 Testing the depth calibration algorithm using a planar surface.

21

5. Transversal Calibration

Transversal calibration refers to the process of converting the known depth values and pixel's indices in a camera into the X and Y real world coordinate system. The steps below explain the proposed transversal calibration algorithm for a one-sensor fringe projection system on a step-by-step basis. This algorithm may be extended to multi-sensor fringe projection system as described in Section 7.

The absolute transversal calibration process starts by determining the centre of the real world coordinates. This is an important first step since the transversal calibration process that is proposed here is absolute. We have used the intersection of three laser beams that are fixed to three perpendicular walls in a room in order to determine this centre as shown in Fig. 3(a).

5.1 Imaging of a printed fringe pattern

A fringe pattern image with a size of 512×512 pixels is constructed with vertical fringes. The spatial period of fringes is set, for example, to 24 pixels per fringe. The spatial period of the two fringes that are close to the centre of the image is set to be double the spatial period of the other fringes (*e.g.*, 48 pixels per fringe). This image is shown in Fig 5(a) and row 256 of this image is shown in Fig. 5(b). Notice the continuity of the phase during the transition from a spatial frequency (*e.g.,* 1/24) to the next (*e.g.,* 1/48). The line that separates both fringes with double spatial period represents the Y axis (the valley point) and this image is used to calibrate the camera's X coordinate.

Similarly, a fringe pattern image is constructed with horizontal fringes. The spatial period of the two fringes close to the centre of the image is again double the spatial period of the other fringes. This image is shown in Fig 5(c). The line that separates both fringes with the double spatial period represents the real world X axis and this image can be used to calibrate the camera's Y coordinate.

Both images shown in Figs. 5(a) and 5(c) are combined using arithmetic addition and the resultant image is shown in Fig. 5(d). The data type for the image shown in Fig. 5(d) is set to be

integer. If the data type were set to byte, then the addition operation may result in clipping (saturation) for values that are larger than "255".

The proposed transversal calibration method can be automated easily to absolute calibrate the X and Y coordinates. This is because the X and Y axes and the calibration centre are determined automatically by the dual fringe pattern image as shown in Fig. 5(d). One the other hand, other traditional calibration methods, such as Tsai [17] and Liu [10], requires human intervention to determine the calibration centre. For example, Tsai method requires using the mouse to click on calibration centre in the chessboard image. This process should be repeated for every calibrated height. This makes using these traditional methods tedious and error prone.

The combined dual fringe pattern image, shown in Fig. 5(d), is printed on a white-planar glass platten. Also, the X and Y axis are marked on the platten with arrows as shown in Fig. 5(d). In the printed fringe pattern used in this experiment, the period of the printed fringe is set to a value of 19 mm and for the double period fringe it is set to 38 mm. This platten is placed at the absolute depth Z=0 by aligning it using the laser beam shown in Fig. 3(b). Also, the other two laser beams shown in Fig. 3(a) are used to align the X and Y axes marked on the platten such that the two laser beams coincide with the X and Y axis (*i.e.,* both arrows in Fig. 5(d)). The laser beams are switched off after finishing the initial alignment process. The platten is then imaged using the camera.

5.2 Processing of the printed fringe pattern image

The capture image is shown in Fig. 5(e) as a 2D intensity image. The captured image is processed using the 2D Fourier transform algorithm explained in [20]. The Fourier transform of the captured image is shown in Fig. 5(f). The spectrum of the horizontal fringes is separated from the spectrum of the vertical fringes. The frequency components that belong to the horizontal fringes are selected and the other components are set to zero. Then the inverse 2D Fourier transform is computed. After that the wrapped phase map is calculated and this is shown in Fig. 5(g). The above process is repeated, but this time for the vertical fringes in the composite pattern and the resultant wrapped phase map is shown in Fig. 5(h).

Typically, the phase values in the wrapped phase map of any fringe pattern have a range of values from $-\pi$ to $+\pi$. However, the wrapped phase values of the double-period fringes are identified and then are multiplied by 2, which results in their range being from -2π to $+2\pi$. This is because the fringes that have double the period of the other fringes have half the phase of the other fringes. This multiplication by "2" is a compensation for this difference. This process is performed on the wrapped phase map shown in Fig. 5(h) and row 256 of the resultant phase map is shown in Fig. 5(i). This process is repeated for the wrapped phase map image shown in Fig. 5(g).

Initially the Y axis is located exactly at the wrap that separates the two double period fringes shown in Fig. 5(h). The value of the phase at this wrap is known to be 2π; hence the location of the Y axis can be determined with sub-pixel accuracy using linear interpolation as explained in the absolute depth calibration section. This process is carried out for all the rows in the image and this produces 512 phase values.

Phase unwrappers typically add or subtract 2π values at the phase wrap locations in order to remove these discontinuities and unwrap the phase distribution, however, as we can see from Fig. 5(i), the phase wraps of the double period fringes have values greater than π, and therefore they must be unwrapped outside the standard phase unwrapper in order for the unwrapping process to perform correctly.

By examining Fig. 5(i) the reader can notice that the first, the second and the third double-period fringe phase wraps have phase jump values of 3π, 4π, and 3π, respectively. The following steps are carried out in order to properly unwrap the wrapped phase shown in Fig. 5(i). The phase wrap locations of the double period fringes are identified by searching the wrapped phase maps for the phase wraps with the greatest spatial period. Then the appropriate phase values are added to these phase wraps. For the example in Fig. 5(i): 3π is added to the first wrap on the left, then 4π is added to the second wrap, then 3π is added to the third wrap. The result of this step is displayed in Fig. 5(j). This process is repeated for all the rows of the wrapped phase map shown in Fig. 5(h).

The phase unwrapping process is continued using a phase unwrapping algorithm such as the reliability sorting phase unwrapper [32] in order to produce a final unwrapped phase map. The two resultant wrapped phase maps are shown in Figs. 5(k) and 5(l). These relative phase maps must next be converted to absolute phase.

All the points in the Y axis are located on the valley of a fringe (*i.e.*, a wrap); hence they should all have close unwrapped phase values, but they may deviate slightly due to noise. The average of these values is calculated to average out such noise. This average is subtracted from the relative unwrapped phase map shown in Fig. 5(k). The resultant phase is absolute and this makes the phase values on the Y axis close to zero.

The period of a fringe on the printed fringe pattern is 18 mm. This means that a 2π phase value is equivalent to 18 mm. So the absolute unwrapped phase image is multiplied by the scale factor $18/2\pi$. This produces an absolute distance map and calibrates the Y coordinate.

The wrapped phase map shown in Fig. 5(g) is processed in similar manner as the phase map shown in Fig. 5(h) in order to calibrate the X coordinate.

The process in the above two sub-sections is repeated for different absolute depth values. In this experiment, absolute depth values with Z=10, 20, 30, 40, …140 mm are used. Notice that the depth values used in the depth calibration must be used in the transversal calibration. Changing the depth values can be carried out either manually or automatically using an elevator table mechanism as described previously.

A lookup table that relates absolute X coordinate values to the depth values for each pixel can then be constructed. This calibration process produces $512 \times 512 = 262,144$ lookup tables, and each lookup table has 15 entries. The relationship between depth and X coordinate for a specific pixel in the camera is shown in Fig. 5(m). Also, the relationship between depth and Y coordinate for a specific pixel is shown in Fig. 5(n).

The above procedures can be carried out to calibrate the X and Y coordinates of the three sensors simultaneously, or one-by-one. These procedures have been used to calibrate the three sensors in Fig. 2(a) system simultaneously and automatically without any manual intervention. The three images captured by these sensors are shown in Figs. 5(e), 5(o) and 5(p).
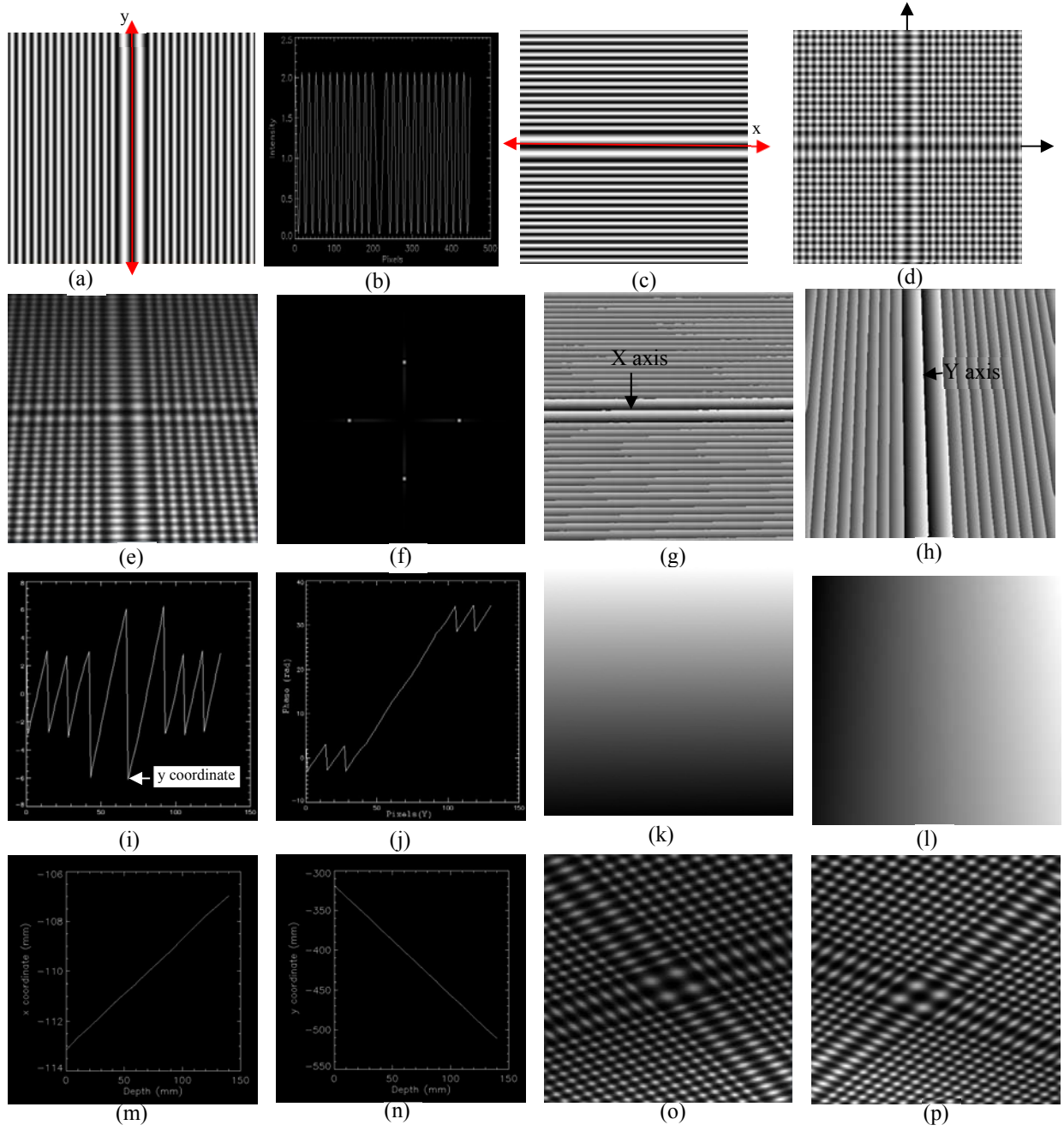
Fig. 5 Absolute transversal calibration of the fringe projection system.

6. Absolute Shape Measurement Using a Single Sensor Fringe Projection System

Fig. 6(a) shows a model object prototype of female human medical breast phantom that is placed on a rectangular flat planar surface at an absolute depth of 7.00 mm. This object is measured using the system's green sensor. The fringe pattern shown in Fig. 3(c) is projected onto the phantom object and the deformed fringe pattern is captured using a camera. The captured fringe pattern is shown in Fig. 6(b). The five-spot image shown in Fig. 3(g) is then projected onto the phantom object and then captured using the camera. The captured image is shown in Fig. 6(c). The deformed fringe pattern is restored to remove the distortions in the source fringe patterns that were added by the spots and then it is analysed using the Fourier transform method. This produces a wrapped phase map which is shown in Fig. 6(d). This phase map is unwrapped and it is shown in Fig. 6(e). This unwrapped phase is converted from relative to absolute using the five spots' centres method. After that the absolute phase is converted to absolute depth using linear interpolation as explained in the depth calibration section.

The depth values for every pixel are known. The depth value and x index for a pixel are used to determine the X real world coordinate. This is carried out by using the X-coordinate lookup table and by employing linear interpolation. The X lookup table is generated during the transversal calibration process as explained in Section 5 and it relates Z to X. For example, two entries to the lookup table are $Z = [0, 10]$ and $X = [-113.157, -112.657]$, which is plotted in Fig. 5(m). Also let the depth for this pixel in the absolute phase of the breast phantom object be $Z = 9$ mm. Then the slope of the line connecting both points has the basic linear equation $x = mz + b$. The slope $m = 0.5$ and $b = -113.157$. The X coordinate for this pixel is thus $0.5(9) - 113.157 = -112.707$ mm. This step is repeated in order to find the Y coordinate for this pixel, but this time using the Y-coordinate lookup table.

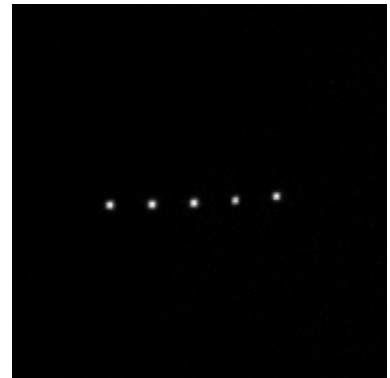This process is repeated to find the X and Y real world coordinates for every pixel in the depth map.

The X and Y absolute coordinates are determined for every pixel in the camera. The 3D shape of the breast phantom is shown in Fig. 6(f). Notice that any camera perspective distortion as is evident in Fig. 6(a) is removed using the transversal calibration as shown in Fig. 6(f).
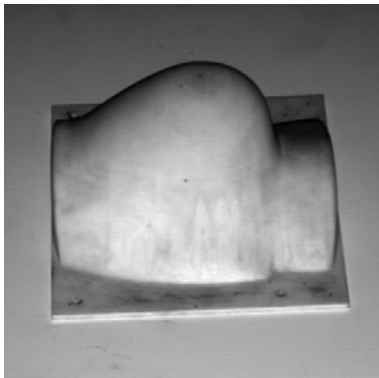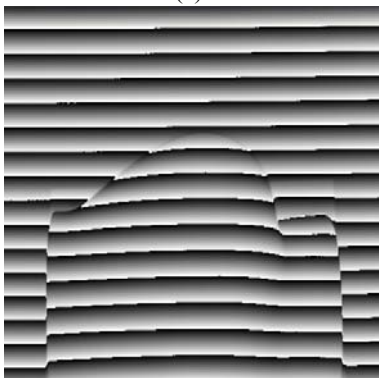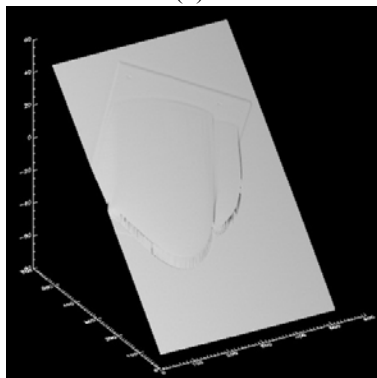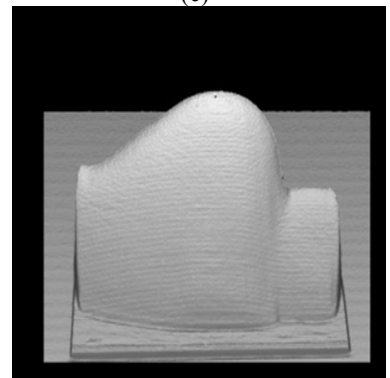
(a)
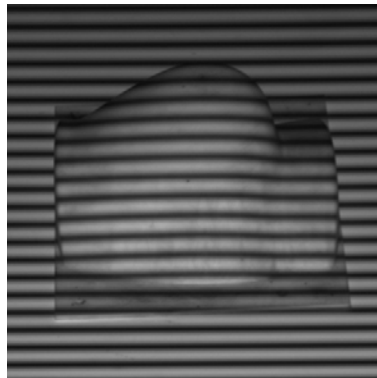
(b)

(c)

(d)

(e)

(f)

Fig. 6 Measurement of a medical human breast phantom using the one-sensor fringe projection system.

7. Absolute Shape Measurement Using a Multi-Sensor Fringe Projection System

One of the advantages of the proposed transversal calibration method is that it provides the multi-sensor fringe projection measurement system with the ability to define a unified transversal coordinate system that can be used by all sensors. This enables the system to easily combine measurements that originate from different sensors and subsequently to combine them into a single object 3D measurement map.

Transversal calibrating one of the sensors using the bidirectional printed fringe pattern that is shown in Fig. 5(d) is described in detail in section 5. When calibrating other sensors for transversal measurement, one must follow the following steps.

1. The printed fringe pattern must be placed in the same location when calibrating different sensors. Any shift in its location will shift the transversal axes and consequently different individual sensors will have slightly shifted transversal axes.

2. Each of the sensors views the bidirectional printed fringe pattern from a different perspective angle, and therefore the fringes might not be running exactly horizontally or vertically, but instead may be running at an angle that is not orthogonal to the system axes. Figs. 5(e), 5(o) and 5(p) demonstrates three images of the same bidirectional fringe pattern as it is viewed by the three different sensors. This imposes slight changes in the procedure for extracting the wrapped phase distribution of the fringe images, which is achieved as follows:

   a. For filtering in the frequency domain, the half-plane filter is rotated at an angle that matches the angle of the fringes.

   b. The location of the exponential filter is relocated so that it is centred at one of the two information peaks. When the fringes in the captured camera images are running horizontally and vertically, as demonstrated in Fig. 5(e), the information peaks of the Fourier spectrum are located at the X and Y axes of the Fourier spectrum. However, when the fringes are running diagonally, , as demonstrated in Figs. 5(o) and 5(e), the information peaks of the Fourier spectrum are located away from the Fourier spectrum's X and Y axes. So the location of the exponential filter should be adjusted accordingly.

29

The medical breast phantom is measured here using the three-sensor fringe projection system. The fringe pattern shown in Fig. 3(h) is projected onto the phantom object using the red sensor projector and the deformed fringe pattern is captured using the red sensor camera, which is shown in Fig. 7(a). The spot's location is highlighted in the image using a red circle that appears here for identification purposes only. This process is repeated for the green and blue sensors and the captured fringe patterns are shown in Figs. 7(b) and 7(c). These three fringe patterns are analysed using the Fourier method for the green sensor that was explained in Section 6. This produces three 3D shape maps of this object and they are shown in Figs. 7(d), 7(e) and 7(f).

Because the transversal coordinates of the three sensors were calibrated simultaneously using the same central X and Y axes, the measurement results of the three sensors precisely and accurately overlay upon each other as shown in Figs. 7(g) and 7(h). Then under a CAD environment, the 3D point clouds were merged and aligned to the reference surface of the breast phantom cast as shown in Fig. 7(i).

A set of Coordinate Measuring Machine (CMM) data that was measured for the breast phantom cast is used here as a reference surface, which was measured using an NVision 3D laser scanner with an overall measurement accuracy of 10 microns [33]. Fig. 7(j) shows a perspective view for the merged three measurement results (in purple) of the breast phantom cast using the three sensor system and its corresponding CMM reference surface (in yellow). Using the CAD environment, the 3D deviation map between the three merged surfaces and the CMM reference surface of the breast cast was calculated and is shown in Fig. 7(k).

7.1 Repeatability test

Ideally, when measuring a static object more than once all measurements should be identical, in other words, the system should be a time-invariant system. However, in reality, the system is not completely time-invariant as some time-variant parameters participate in the production of the final measurement. Examples of such time-variant parameters are the camera's random noise and projector vibration.

In order to provide quantitative measures of the system's repeatability, multiple objects, mostly flat surfaces, were each measured 100 times using the three system sensors. Differences between consecutive measurements for the same object were then computed and analysed. Table 1 provides the results of these tests. Table 1 shows that the blue sensor has the best repeatability performance of the three sensors, followed by the red sensor and lastly the green sensor.

Conclusions

This paper proposes automatic absolute depth and transversal calibration algorithms. These algorithms can be used with single or multi-sensor fringe projection systems. Also, the optical setup of cameras and projectors is arbitrary; since both methods do not any put restrictions on the optical setup. The calibration is carried out for every pixel in both cameras and projectors, so dead or noisy pixels will not affect the accuracy of the calibration of other pixels. The 3D measurement data produced using both algorithms have been compared with CMM data and the three sigma accuracy was found to be less than 0.5 mm.
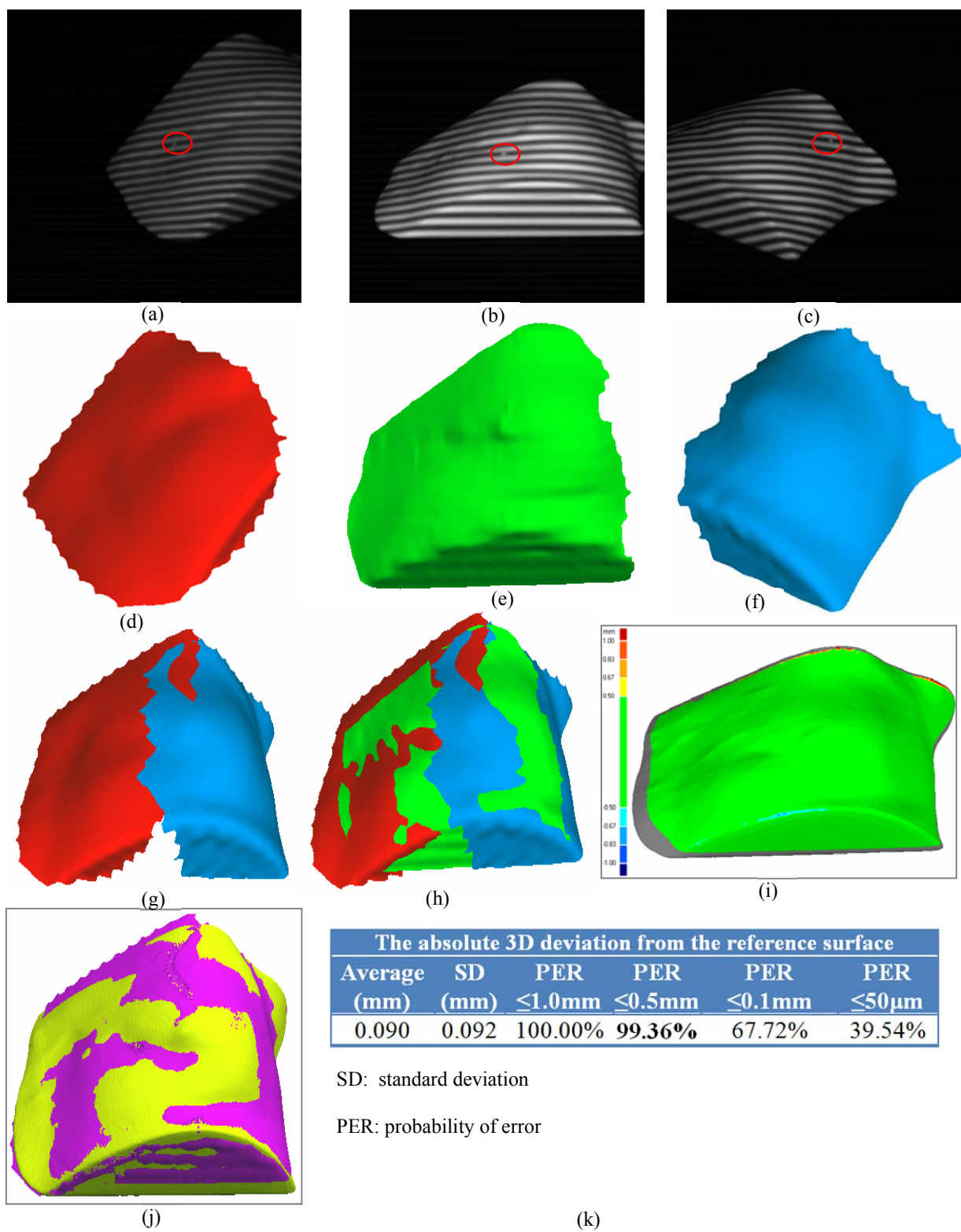
The absolute 3D deviation from the reference surface					
Average (mm)	SD (mm)	PER ≤1.0mm	PER ≤0.5mm	PER ≤0.1mm	PER ≤50μm
0.090	0.092	100.00%	99.36%	67.72%	39.54%

SD: standard deviation

PER: probability of error

Fig. 7 Measuring the breast phantom using the three-sensor fringe projection system.

	Blue Sensor	Green Sensor	Red Sensor
Mean absolute depth measurement difference (mm)	0.136	0.278	0.201
Standard deviation of depth measurement difference (mm)	0.110	0.219	0.151
Mean absolute transversal measurement difference (mm)	0.17800	0.25800	0.29200
Standard deviation of transversal measurement difference (mm)	0.135	0.281	0.225

Table 1: Repeatability testing for the three system sensors.

References

1. Emanuele Zappa, Giorgio Busca, Static and dynamic features of Fourier transform profilometry: A review, Optics and Lasers in Engineering, Volume 50, Issue 8, August 2012, Pages 1140-1151.

2. Lilley F., Lalor MJ. and Burton DR. (2000). Robust fringe analysis system for human body shape measurement. *Optical Engineering*. Vol. 39, 187-195.

3. Giorgio Busca, Emanuele Zappa, Sensitivity analysis applied to an improved Fourier-transform profilometry, Optics and Lasers in Engineering, Volume 49, Issue 2, February 2011, Pages 210-221.

4. Zhu F., Shi H., Bai P. and He X. (2011). Three-dimensional shape measurement and calibration for fringe projection by considering unequal height of the projector and the camera. *Applied Optics*. Vol. 50, Issue 11.

5. Jia P., Kofman J. and English C. (2007). Comparison of linear and nonlinear calibration methods for phase-measuring profilometry. *Optical Engineering*. Vol. 46, Issue. 4.

6. I. Léandry, C. Brèque, V. Valle, Calibration of a structured-light projection system: Development to large dimension objects, Optics and Lasers in Engineering, Volume 50, Issue 3, March 2012, Pages 373-379.

7. Tian A., Jiang Z. and Huang Y. (2006). A flexible new three-dimensional measurement technique by projected fringe pattern. Optics and Lasers Technology Vol. 38, 585-589.

8. Huafen Luo, Jing Xu, Nguyen Hoa Binh, Shuntao Liu, Chi Zhang, Ken Chen, A simple calibration procedure for structured light system, Optics and Lasers in Engineering, Volume 57, June 2014, Pages 6-12.

9. E. Zappa, G. Busca, Fourier-transform profilometry calibration based on an exhaustive geometric model of the system, Optics and Lasers in Engineering, Volume 47, Issues 7-8, July-August 2009, Pages 754-767.

10. Liu H., Hung W., Su W., Reichard K. and Yin S. (2003). Calibration-based phase-shifting projected fringe profilometry for accurate absolute 3D surface profile measurement, *Optics Communications.* Vol. 216, 65–80.

11. Argenio CD. and Leo G. (2009). A simplified procedure for the calibration of a fringe pattern profilometer. *IEEE Instrumentation and Measurement Technology Conference,* 652-657.

12. Jesús Villa, María Araiza, Daniel Alaniz, Rumen Ivanov, Marvin Ortiz, Transformation of phase to (x,y,z)-coordinates for the calibration of a fringe projection profilometer, Optics and Lasers in Engineering, Volume 50, Issue 2, February 2012, Pages 256-261.

13. Anchini R., Leo D. and Liguori C. (2009). A New Calibration Procedure for 3-D Shape Measurement System Based on Phase-Shifting Projected Fringe Profilometry. *IEEE Transactions on Instrumentation and Measurement.* Vol. 58, Issue 5.

14. Zhang X., Yuchi L., Meirong Z., Xiaobong, N. and Yinguo, H. (2005). Calibration of a fringe projection profilometry system using virtual phase calibrating model planes. *Journal of Optics A: Pure and Applied Optics.* Vol. 7, Issue192.

15. D'Argenio C., Leo DG., Liguori C. and Paolillo A. (2009). A simplified procedure for the calibration of a fringe pattern profilometer. *International Instrumentation and Measurement Technology Conference*, Singapore 5-7 May 2009.

16. E. Zappa, G. Busca, P. Sala, Innovative calibration technique for fringe projection based 3D scanner, Optics and Lasers in Engineering, Volume 49, Issue 3, March 2011, Pages 331-340.

17. Tsai RY. (1987). A versatile camera calibration technique for high-accuracy 3D machine vision metrology using off-the-shelf TV cameras and lenses. *IEEE Journal of Robotics and Automation.* RA-3, 323-344.

18. Salvi J., Armangue X. and Batlle J. (2001). A comparative review of camera calibrating methods with accuracy evaluation. *Pattern Recognition.* Vol. 35, 1617-1635.

19. Stinik R., Kujawinska M. and Woznicki J. (2001). Digital fringe projection system for large-volume 360-deg shape measurement, Optical Engineering, Vol. 41, pp443-449.

20. Burton DR. and Lalor MJ., "Multichannel Fourier fringe analysis as an aid to automatic phase unwrapping," Applied Optics Vol. 33, Issue 14, pp. 2939-2948 (1994).

21. http://www.omegafilters.com/. Accessed on 7/7/2015.

22. Creath K., (1993) "Temporal phase measurement methods," chapter 2 of "*Interferogram analysis: digital fringe pattern measurement techniques*," Edited by Robinson WR. and Reid GT., Institute of Physics Publishing, Bristol and Philadelphia, pp. 94-140.

23. Ghiglia D, Pritt M., Two-Dimensional Phase Unwrapping Theory, Algorithms and Applications, John Wiley & Sons, 1998.

24. Qudeisat M., Gdeisat M., Burton D., Lilley F., "A simple method for phase wraps elimination or reduction in spatial fringe patterns," Optics Communications, Volume 284, Issue 21, 1 October 2011, Pages 5105–5109.

25. Yu C., Peng Q., "A correlation-based phase unwrapping method for Fourier-transform profilometry," Optics and Lasers in Engineering, Volume 45, Issue 6, June 2007, Pages 730-736.

26. Oscar Dalmau, Mariano Rivera, Adonai Gonzalez, Weighted robust Basis Function for phase unwrapping, Optics and Lasers in Engineering, Volume 69, June 2015, Pages 13-19.

27. Yuangang Lu, Wancheng Zhao, Xuping Zhang, Weihong Xu, Guoliang Xu, Weighted-phase-gradient-based quality maps for two-dimensional quality-guided phase unwrapping, Optics and Lasers in Engineering, Volume 50, Issue 10, October 2012, Pages 1397-1404.

28. Yi Ding, Jiangtao Xi, Yanguang Yu, Fuqin Deng, Absolute phase recovery of three fringe patterns with selected spatial frequencies, Optics and Lasers in Engineering, Volume 70, July 2015, Pages 18-25

29. MATLAB image processing toolbox, www.mathworks.com. Accessed on 7/7/2015.

30. 5.12 Parker Automation Website http://www.parkermotion.com/manuals/Digiplan/ViX-IM_UG_2-04.pdf. Accessed on 7/7/2015.

31. R. Gonzalez and R. Woods R. (2008). Digital Image Processing, Pearson Education, third edition.

32. Miguel Arevallilo Herráez, David R. Burton, Michael Lalor, and Munther Gdeisat, "Fast two-dimensional phase-unwrapping algorithm based on sorting by reliability following a noncontinuous path," Applied Optics Vol. 41, Issue 35, pp. 7437-7444 (2002).

33. NVISION. 2008. NVision 3D laser scanner [Online]. nvision3d.com. Available: http://www.nvision3d.com/nvision-products.html, Accessed 7th July 2015.